NASA Technical Memorandum 4419

# Transition Aerodynamics for 20-Percent-Scale VTOL Unmanned Aerial Vehicle

Kevin J. Kjerstad and John W. Paulson, Jr.

APRIL 1993

NASA Technical Memorandum 4419

# Transition Aerodynamics for 20-Percent-Scale VTOL Unmanned Aerial Vehicle

Kevin J. Kjerstad and John W. Paulson, Jr.
*Langley Research Center*
*Hampton, Virginia*

## Abstract

*An investigation was conducted in the Langley 14- by 22-Foot Subsonic Tunnel to establish a transition data base for an unmanned aerial vehicle utilizing a powered-lift ejector system and to evaluate alterations to the ejector system for improved vehicle performance. The model used in this investigation was a 20-percent-scale, blended-body arrow-wing configuration with integrated twin rectangular ejectors. The test was conducted from hover through transition conditions with variations in angle of attack, angle of sideslip, free-stream dynamic pressure, nozzle pressure ratio, and model ground height. Force and moment data along with extensive surface pressure data were obtained. A laser velocimeter technique for measuring inlet flow velocities was demonstrated at a single flow condition, and also a low order panel method was successfully used to numerically simulate the ejector inlet flow.*

## Introduction

Unmanned aerial vehicles (UAV's) have become increasingly valuable as decoys and frontline reconnaissance platforms as evidenced in the recent Persian Gulf war (ref. 1). An advantage of these vehicles is the ability to launch them and to recover them anywhere in the field of operation. However, the low vehicle gross weight and small size of the vehicle severely limits the amount of on-board instrumentation, the operating range, and loiter time. Furthermore, some UAV's require specialized equipment for launch and recovery which can restrict their ease of operation. To overcome these shortfalls, the Boeing Company has proposed a much larger UAV which utilizes a powered-lift ejector system, like the E-7A concept (ref. 2), to provide vertical takeoff and landing capabilities.

As the Lewis Research Center has completed a full-scale static ejector test (ref. 3), the current test was conducted as a joint effort between the Boeing Company and the Langley Research Center to investigate the performance of an integrated airframe-ejector system. A 20-percent-scale model of an envisioned UAV was tested from hover through transition conditions to establish a powered-lift data base and to evaluate lift augmentation, induced drag, and pitching-moment sensitivities to ejector variations. During the test, laser velocimeter techniques to measure inlet flow velocities were demonstrated, and inlet flow data for validation of computational fluid dynamics (CFD) methods were obtained.

The 20-percent-scale model had a blended-body, arrow-wing shape with a leading-edge sweep of 60° and twin rectangular ejectors centered about the moment reference center of the vehicle. The model also had wing-tip elevons, leading-edge vortex flaps, and a removable vertical V-tail. The ejector system diffuser exit area, diffuser turning vanes, diffuser streamwise skew angle, ejector centerline dam, and inlet doors were varied.

The investigation was conducted over a free-stream dynamic pressure range of 0 to 48 psf. The primary nozzle pressure ratio representing power off and power on conditions varied from 1 to 3. Angle of attack was varied from 0° to 26°, and sideslip sweeps were conducted from 20° to −20° at constant values of $\alpha$ of 0° and 10°. The model ground height varied from 2.5 to 72 in. above the tunnel floor.

The purpose of this report is to present general results obtained from analysis of the test data and CFD simulations which may be beneficial to future design efforts of air vehicles with ejector systems. This report does not contain detailed analysis of all data created during this specific test, nor present the entire integrated ejector data base.

## Symbols

The force, moment, and pressure data from wind-on runs were reduced to standard coefficient form with a moment reference center located 37.2 in. aft of the leading-edge apex along the intersection of the vertical and horizontal symmetry planes. All longitudinal coefficient data were computed about the stability-axis system, whereas all lateral-directional data and all noncoefficient data were computed about

the body-axis system. For convenience, the drag coefficient nomenclature has been retained in sideslip.

| | |
|---|---|
| $b$ | wing span, in. |
| BL | buttline, in. |
| $\overline{c}$ | mean aerodynamic chord, in. |
| CFD | computational fluid dynamics |
| $C_D$ | drag coefficient, $\frac{D}{q_\infty S}$ |
| $C_L$ | lift coefficient, $\frac{L}{q_\infty S}$ |
| $C_l$ | rolling-moment coefficient, $\frac{M_X}{q_\infty S b}$ |
| $C_m$ | pitching-moment coefficient, $\frac{M_Y}{q_\infty S \overline{c}}$ |
| $C_n$ | yawing-moment coefficient, $\frac{M_Z}{q_\infty S b}$ |
| $C_p$ | pressure coefficient, $\frac{p - p_\infty}{q_\infty}$ |
| $C_{p,e}$ | pressure coefficient referenced to isentropic throat conditions, $\frac{p - p_e}{q_e}$ |
| $C_Y$ | side-force coefficient, $\frac{\text{Side force}}{q_\infty S}$ |
| $D$ | drag force, lb |
| $\Delta D$ | ejector-induced drag increment, $(D)_{\text{wind on, power on}} - (D)_{\text{wind on, power off}} - (D)_{\text{wind off, power on}}$ |
| $F$ | primary nozzle thrust force, lb |
| FS | fuselage station, in. |
| $F_A$ | axial force, lb |
| $F_N$ | normal force, lb |
| $F_S$ | side force, lb |
| HGT | model height (as measured from front of ejector skirt to tunnel floor), in. |
| $L$ | lift force, lb |
| LV | laser velocimetry |
| $L_o$ | lift force with wind off and power on, lb |
| $\Delta L$ | ejector-induced lift increment, $(L)_{\text{wind on, power on}} - (L)_{\text{wind on, power off}} - (L)_{\text{wind off, power on}}$ |
| $M_X$ | rolling moment, in-lb |
| $M_Y$ | pitching moment, in-lb |
| $\Delta M_Y$ | ejector-induced pitching-moment increment, $(M_Y)_{\text{wind on, power on}} - (M_Y)_{\text{wind on, power off}} - (M_Y)_{\text{wind off, power on}}$ |
| $M_Z$ | yawing moment, in-lb |
| $\dot{m}_T$ | theoretical mass-flow rate, slugs/sec |
| NPR | average primary nozzle pressure ratio, $p_t/p_\infty$ |
| $p$ | surface static pressure, psf |
| $p_e$ | computed isentropic throat static pressure, psf |
| $p_t$ | average nozzle total pressure, psf |
| $p_\infty$ | free-stream static pressure, psf |
| $q_e$ | computed isentropic throat dynamic pressure, psf |
| $q_{\text{jet}}$ | average primary nozzle dynamic pressure, psf |
| $q_\infty$ | free-stream dynamic pressure, psf |
| Re $\overline{c}$ | Reynolds number, based on mean aerodynamic chord |
| $S$ | reference area, in$^2$ |
| UAV | unmanned aerial vehicle |
| $V_e$ | $= \sqrt{q_\infty / q_{\text{jet}}}$ |
| $V_{\text{jet}}$ | average primary nozzle jet velocity, ft/sec |
| $V_\infty$ | free-stream velocity, ft/sec |
| WL | waterline, in. |
| $x, y, z$ | Cartesian coordinate system |
| $\alpha$ | angle of attack, deg |
| $\beta$ | angle of sideslip, deg |
| $\delta_v$ | diffuser turning-vane deflection, deg |
| $\Phi$ | augmentation ratio |

## Model Description

The model used in this investigation was a 20-percent-scale arrow wing with twin rectangular ejectors integrated into the blended body of the configuration. A three-view sketch of the model and a photograph of the model installed in the 14- by 22-Foot Subsonic Tunnel are shown in figure 1. The model was fabricated and supplied by the Boeing Company. The arrow-wing planform

of the model had a leading-edge sweep of 60° and root to tip trailing-edge sweeps of −37.5°, 60°, and −37.5°. Biconvex-shaped airfoil sections were used to produce sufficient cross-sectional area distribution (fig. 2) to immerse the entire ejector system into the blended wing-body. The model also had split wingtip elevons, leading-edge vortex flaps, and a removable vertical V-tail, which were tested, but the effectiveness of these components will not be presented in this report. During all runs with wind on, transition strips of No. 60 carborundum grit were in place 0.5 in. aft of the leading edge.

The ejector system (fig. 3) was based on a design of the Boeing Company which was evaluated in a full-scale static test at the Lewis Research Center (ref. 3). The system consisted of a single secondary plenum that supplied air to 10 primary plenums on each side. Each primary plenum fed three notched-cone primary nozzles (ref. 4) whose exit planes were located 1.78 in. above the ejector throat. The area of the ejector throat was fixed at 84.48 in., but the diffuser exit area could be varied to optimize the ejector efficiency by changing the diffuser sidewall cant angle. For all data presented, the diffuser exit area, optimized for the baseline configuration, was 141.08 $in^2$ which results in a diffuser-to-throat area ratio of 1.67.

Variations to the baseline ejector system included rotatable primary plenum/nozzle components which were deflected with a skewed diffuser box to investigate effects of streamwise diffuser skew in an integrated ejector configuration (fig. 4(a)). In addition, 2-in. removable diffuser turning vanes with 50 percent chord flaps were installed in the diffuser box (fig. 4(b)) to investigate thrust vectoring effectiveness. Each diffuser box had nine full ejector-span turning vanes located 7.5 in. below the ejector throat and midway between the primary plenums. Also, the two forward nozzles on each ejector were plugged and a splitter plate was added to each ejector (fig. 4(a)) to investigate possible alternatives for pitch control. Finally, in an attempt to trap the centerline fountain which forms between the two ejectors when in ground effect, forward and aft endplate extensions (fig. 5) spanning the distance between the diffuser endplates were investigated.

Three ejector inlet door designs were tested with an operating ejector. In one design, the entire door rotates about the outboard inlet lip to slightly past a vertical position. In a second design, the ejector door was split in two with one half opening outboard and the other half folding into the centerline. Finally, a multisegmented door design that folds inboard to form an aerodynamically shaped centerbody was tested. Sketches of the three door designs are shown in figure 6.

The fully metric model was internally mounted on a standard six-component strain-gage balance which was supported on a bent air sting (ref. 5). High-pressure air was supplied to the ejector system through the air sting which has an internal, free floating, coiled air line to provide a nonmetric bridge across the balance for the air supply and to minimize the load interactions between the air line and balance.

A list of other pertinent model information is given in table I.

## Instrumentation and Data Reduction

The six-component balance used to measure the model forces and moments had load capacities and guaranteed accuracies shown in the following table:

| Force or moment | Maximum load capacity | Load accuracy | Coefficient accuracy[a] |
|---|---|---|---|
| Axial . . . | ±500 lb | ±2.5 lb | ±0.012 |
| Side . . . | ±1800 lb | ±9.0 lb | ±0.044 |
| Normal . . | ±3000 lb | ±15.0 lb | ±0.074 |
| Rolling . . | ±7500 in-lb | ±37.5 in-lb | ±0.003 |
| Pitching . . | ±10000 in-lb | ±50.0 in-lb | ±0.006 |

[a]Reflection of only the balance sensitivity and is based on $q_\infty = 12$ psf.

Balance loads created by the high-pressure air system were removed from the force and moment data by calibration and pressure tares. Prior to the test, a calibration of the balance and air line interactions for an unpressurized system was obtained and added as corrections in the data reduction software. An air sting pressure tare, used to account for balance loads due to pressurizing the air supply system, could not be made at the start of the test because of the ejector system design. Therefore, a pressure tare from a previous test (ref. 6) utilizing the same air sting and balance was used. During posttest model disassembly, an air sting pressure tare was taken, and negligible differences were found between the two tares. Therefore, no additional corrections to the data were made.

Additional model instrumentation include 170 static pressure ports located on the inlet surfaces and 208 static pressure ports on the wing-body surfaces. Surface pressures were measured with 5-psid electronically scanned pressure modules. Although detailed analysis of the pressure data is not presented

in this report, some of the inlet pressure data are used for comparative purposes with CFD results.

Two 50-psi differential pressure transducers, used to measure the static pressure in the secondary plenum, were calibrated at the beginning of the test. The average of these two pressure transducers was used to compute the total pressure at the primary nozzle exits and to calculate NPR and $V_{\text{jet}}$ of the primary nozzles during the test. Furthermore, pressure surveys of the diffuser exit were used to determine the total mass flow through the ejector at various values of NPR. These data were then used to calculate the isentropic flow condition at the ejector throat.

For all power-on runs, the ejector augmentation ratio $\Phi$ was calculated by the following equation:

$$\Phi = \frac{F_N}{F} = \frac{F_N}{\dot{m}_T V_{\text{jet}}}$$

Typically, measured mass flow is used in the calculation of $\Phi$, but because of instrumentation problems with the air supply system, theoretical mass flow had to be used. This procedure should make the resulting $\Phi$ slightly conservative because the theoretical mass flow assumes a unity discharge coefficient and actual nozzle discharge coefficients are around 0.95.

When the ejector operated during the test, significant variations in the force and moment data along with a continuous model vibration were noted. These phenomena could be the result of unsteady mixing of air in the ejector which alters its performance. Numerous changes were made to the ejector system to minimize this problem; however, it could not be completely eliminated. Thus, the number of data samples per point was increased from 20 to 60 for a better statistical average. Repeat runs taken throughout the test still show significant data scatter. The actual data are plotted as symbols, and least-squares curves through the data are used to indicate reasonable trends. The force and moment data at $q_\infty$ = 3 psf varied widely because of unsteady ejector performance and extremely light balance loads; therefore, they are not presented in this report.

## Test Conditions and Procedures

The test was conducted in the Langley 14- by 22-Foot Subsonic Tunnel configured with an open test section to reduce the interference effect of the ejector flow field. The model was tested from hover through transition conditions with variations in tunnel dynamic pressure, primary nozzle pressure ratio, angle of attack, sideslip angle, and ground height.

For runs with wind on, tunnel dynamic pressure was varied from 3 to 48 psf, corresponding to a Reynolds number range of $1.1 \times 10^6$ to $4.5 \times 10^6$ based on $\bar{c}$, with most of the data obtained at the nominal transition condition of 12 psf. At constant tunnel dynamic pressure, the effects of the ratio $V_\infty/V_{\text{jet}}$ were examined by varying NPR over a range from 1 to 3. Due to insufficient mass-flow rates, the designed operating condition for the ejector system, NPR = 3, could not be obtained with all the primary nozzles flowing. Therefore, most of the data obtained with the ejector operating are at NPR = 2.5.

During the test, an internally mounted inclinometer was used to measure angle of attack which varied from 0° to 26°. Sideslip angles, measured by a calibrated turntable, were swept from 20° to −20° at constant $\alpha = 0°$ and 10°. Typically, $\alpha$ and $\beta$ sweeps were conducted at a constant ground height as measured by a mast encoder referenced to the bottom of the forward diffuser skirt. However, near the end of the test, loss of control of the height mechanism resulted in ground height variations with changes in $\alpha$ (i.e., as $\alpha$ increased, ground height increased). Ground height sweeps from 2.5 to 72 in. were conducted at constant $\alpha = 0°$ and 10° and $\beta = 0°$. From initial height sweeps, the nominal out of ground effect height was chosen to be 32 in.

A procedure for measuring inlet horizontal and vertical velocity components with a two-component laser velocimeter system (ref. 7) was investigated. The laser velocimeter system operated in backscatter mode, and the inlet flow was seeded with 6-mm polystyrene balls from a remote control seeding rig located upstream of the wind-tunnel contraction section.

Because the system measures two dimensions, only the inlet symmetry flow plane could be measured with confidence. To establish the symmetry flow plane, cross-flow planes near the front and back of the ejector inlet were mapped to a height of negligible free-stream velocity change. From the vertical velocity distribution at each mapped plane, the symmetry flow plane was established to be approximately a vertical plane centered over the inlet at BL = 6.0 in. LV data were then obtained along this vertical plane at a single flow condition of $\alpha = 0°$, $q_\infty$ = 3 psf, NPR = 2.5, and HGT = 32 in.

## Discussion of Results

### Baseline

Static results for the baseline ejector configuration are shown in figures 7 through 9. In figure 7, the effects of increasing NPR on longitudinal forces and

moment at $\alpha = 0°$ and $10°$ are shown. Because the data are referenced to the body axis, they should not vary with $\alpha$; therefore, the variation is representative of the data scatter for power on.

Longitudinal forces and moment versus ground height are presented in figure 8. The general decrease in normal force with decreasing ground height for both values of $\alpha$ is caused by greater amounts of lower surface flow being entrained into the exhaust flow creating a suck down effect. Because more surface area aft of the moment reference center is influenced by the ejector exhaust, additional nose-up pitching moment is created. Some of the loss in normal force is also caused by back pressurizing the ejector system which reduces its performance. For $\alpha = 10°$, the increasing normal force below HGT = 7 in. is caused by trapping the aft exhaust flow between the aft portion of the model and the ground. The trapped flow creates a high-pressure region. This condition also produces a decreasing nose-up pitching-moment trend. Ejector augmentation (fig. 9) has the same trends as the normal-force plot. The considerable decrease in $\Phi$ between $\alpha = 0°$ and $10°$ is attributed to a reduced centerline fountain effect (fig. 5) and to the difference in ground proximity of the aft end of the model as model height is measured relative to the forward ejector skirt.

The wind-on aerodynamic characteristics of the baseline configuration are shown in figures 10 through 16. The out of ground effect variations in longitudinal aerodynamic coefficients with $\alpha$ for several combinations of NPR and $q_\infty$ are presented in figure 10. Even though the ejectors are centered about the data reference center, nose-up pitching moment is generated with power on because turning the inlet streamtube into the ejector inlet creates a low pressure region forward of the moment reference center between the leading edge and inlet. As expected, increasing $q_\infty$ while holding NPR constant decreases the power effect on the coefficients. From the power-off runs, it is apparent that Reynolds number effects are negligible over the range tested.

Figure 11(a) shows the variation of baseline longitudinal aerodynamic coefficients with NPR. The nonlinear increase in $C_L$ and $C_m$ is a result of increased upper surface flow entrainment with increasing NPR. As NPR increases, the upper surface flow entrainment pattern extends further aft which results in a flattening of the $C_m$ curve. Also as NPR increases, the ejector exhaust flow penetrates farther away from the body before it is turned downstream by the momentum of the free stream which produces additional drag. Figure 11(b) shows the ejector-induced increments in the longitudinal direction as described in reference 8. Like the previous results (ref. 8), the induced aerodynamics generate an increase in drag and nose-up pitching moment because of turning of the inlet streamtube into the ejectors. But unlike results from reference 8, the induced effects on the planform shape produce a positive lift increment which increases with increasing $V_e$.

The effects of ground height on the longitudinal aerodynamics coefficients at $q_\infty = 12$ and 24 psf and NPR = 2.5 are shown in figure 12. As with wind off, lift decreases with reduced HGT, but unlike wind off, nose-up pitching moment decreases. This decrease is caused by the lower surface pressure field being shifted rearward by the free stream and the fountain center moving aft of the moment reference center. The differences in the pressure forward and aft of the ejector exit contribute to the substantial decrease in $C_D$.

Variations in the baseline aerodynamics due to sideslip are shown in figures 13 through 16. With power on or off, the longitudinal aerodynamic coefficients for $\alpha = 0°$ and $10°$ (figs. 13 and 14) are almost unaffected by $\beta$. As seen in figures 15 and 16, the vehicle is directionally unstable, but has positive effective dihedral. In general, powered effects significantly increase the influence of $\beta$ on the lateral-directional coefficient.

### Variations in the Baseline Configuration

Alterations to the baseline ejector configuration that predominately affected the augmentation of the ejector are presented in figures 17 through 21. As shown in figures 17 and 18, removing the forward endplates of the diffuser significantly reduces $C_D$ for $C_L$ below 1.8 at the cost of decreased lift and augmentation.

A reduction in nose-up pitching moment also occurs. With the forward endplates removed, the lower surface flow in front of the ejectors is entrained directly into the exhaust flow. The entrainment creates a stronger negative pressure in this region. However, some lift loss may be attributed to degraded ejector-flow mixing caused by a shorter diffuser length when the endplates are removed.

In an effort to reduce drag without significant lift losses, the primary nozzles and diffusers were skewed 10° downstream (see fig. 4). Also, the forward and aft endplates were extended to the centerline to create a dam for capturing the ejector fountain formed in ground effects (fig. 5). Figures 19 and 20 show the effect of these changes on $\Phi$ at varying ground heights for $\alpha = 0°$ and $10°$. For both values of $\alpha$, $\Phi$ increases with the diffusers skewed and the

centerline dam in place. For out of ground effects and power on (fig. 21), there is a small decrease in lift with the diffusers skewed which diminishes as $\alpha$ increases because the thrust vector is rotating into the lift direction. A similar effect, but to a lesser degree, is seen with the centerline dams in place. The lift loss due to rotating the thrust vector out of the lift direction is not significant because the induced lift created by the inlet flow remains essentially the same. Because skewing the diffusers results in thrust vectoring and reducing exhaust blockage of the free-stream flow, a large drag reduction is obtained.

Inclusion of door-open ejector inlets on an air vehicle tends to decrease the ejector performance by inhibiting inlet flow entrainment. An investigation was conducted to determine if a less degrading door-open design existed. As described in the section "Model Description," three door-open combinations were tested: an outboard door, a split inboard/outboard door, and an aerodynamically shaped centerbody door. Figures 22 through 27 show the effects of these door-open designs on $\Phi$ and the general vehicle performance. As shown in figure 22, the reduction in static lift for the door off increases with NPR for two of the door designs tested. However, examination of the normal force plot reveals a nearly unchanged static lift for the centerbody door design. Figure 23 shows similar trends for $\Phi$ in ground effects at $\alpha = 0°$. At $\alpha = 10°$ (fig. 24), an actual increase in $\Phi$ is observed for the centerbody design when in ground effects. The aerodynamically shaped centerbody (fig. 6) efficiently splits the centerline inlet flow and creates a larger low-pressure region between the ejectors than the low-pressure region created with the no door configuration.

With wind on, power off, and out of ground effects (fig. 25), the outboard and inboard/outboard door designs produce little change in $C_m$ and slightly alter the lift-curve slope which is almost within the stated accuracy of the balance. However, the centerbody design produces a noteworthy increase in $C_L$. With power on, a substantial lift loss and drag increase is incurred from the inboard/outboard door design. Because most of the induced lift loss occurs near the inboard leading edge, $C_m$ also decreases. Although not as severe, the outboard door design has similar effects. For the centerbody design, $C_L$ is only slightly different than for the doors-off design at low values of $\alpha$; however $C_L$ decreases with increasing $\alpha$. The increase in $C_D$ for the centerbody design is slightly greater than the outboard door design, although some of the additional drag could be eliminated with further refinement to the centerbody door design.

The effect of inlet-door design on the aerodynamic characteristics with sideslip is shown in figures 26 and 27. In the longitudinal direction, the trends are essentially the same as those for the baseline; except for $C_n$, little difference in the lateral-directional data is shown in figure 27. Directional stability for the outboard and inboard/outboard door designs is significantly degraded. However, the centerbody door design shows some improvement over the baseline directional stability.

Results of alterations to the ejector system for producing thrust-induced longitudinal and directional control are shown in figures 28 through 35. For wind off (fig. 28), installation of diffuser turning vanes degraded ejector augmentation with little effect on axial force or pitching moment. Deflecting the turning vanes downstream produces significant forward thrust, whereas deflecting them upstream produces equivalent amounts of drag. For both directions, the deflections produce disappointingly small amounts of pitching-moment control and dramatically reduced $\Phi$. However, the uncoupled effect on lift and pitching moment of the turning vanes may be beneficial for forward acceleration of the vehicle when transitioning from hover to forward flight.

Figure 29 shows the effect of turning vane installation on the longitudinal aerodynamics with wind on. As for wind off, turning vane installation had no effect on pitching moment but did increase drag with power on. Surprisingly, vane installation increased $C_L$ for power off and only slightly altered the lift-curve slope with power on.

For turning vane deflections with wind on (fig. 30), the diffuser forward endplates were removed. Deflection of the turning vanes affected $C_D$ and $C_m$ similar to that for wind off. However at higher values of $\alpha$, $C_L$ actually increases for the positive turning vane deflections like it increases for the skewed diffuser configuration.

Effect of unsymmetrical turning vane deflections on the vehicle performance in ground effects with wind off is shown in figures 31 and 32. Longitudinally, only the largest turning vane deflection, $\delta_v = +20/-20$, has a significant effect on the data. As seen in figure 32, the unsymmetrical vane deflections produce a considerable amount of directional control with little roll coupling and no variation in side force. The results are basically the same out of ground effect with wind on (figs. 33 and 34).

In an attempt to reduce the nose-up pitching moment of the baseline configuration with wind and power on, the two forward primary plenums on each of the ejectors were plugged. Also, splitter plates

(fig. 5) were added to the plugged nozzle configuration to further limit flow entrainment forward of the inlet and to provide a channel for venting the lower surface high pressure to the upper surface low pressure region. For both configurations, the ejector diffusers were skewed 10° downstream. For the plugged nozzles alone, the ground height varied from 4.5 in. at $\alpha = 2°$ to 56.5 in. at $\alpha = 16°$ because of tunnel hardware problems. Figure 35 shows the effects on the longitudinal aerodynamics of the nozzles plugged and the nozzles plugged with the splitter plates added. The nose-up pitching moment is reduced by an equivalent amount with or without the splitter plates (the plugged nozzle alone is in ground effects at low values of $\alpha$). This seems to indicate the splitter plates did not perform as expected and may need to be extended farther above the primary nozzles. Since $C_m$ is not affected by increasing NPR to 3, the lift losses obtained with the plugged nozzles may be recovered by increasing NPR the required amount.

## Description of Numerical Method

The low-order panel code VSAERO (ref. 9) was used to model the ejector configuration with the inlet flowing. In VSAERO, the linearized potential equations for an incompressible, irrotational flow are solved by using piecewise constant singularity panels with Neumann and Dirichlet boundary conditions. The method incorporates compressibility corrections, an iterative wake relaxation scheme, and a coupled integral boundary-layer method in which the boundary-layer displacement effects are included in the potential equations as source transpiration.

Discretization of the surface geometry into quadrilateral panels for ejector configurations was facilitated by using the grid generation code, Gridgen (ref. 10). The paneling of the ejector configuration is shown in figure 36. It consisted of 1772 panels of which 812 panels were used to create the inlet surface definition.

The ejector inlet flow was simulated by setting a constant normal velocity on the flux control panels (fig. 36) to match the incompressible mass flow through the inlet which was calculated from the experimental data. Because of the physical complexity, no attempt was made to accurately model the ejector exhaust flow. However, the induced effects of the ejector exhaust flow on the upper surface flow field were investigated by modeling the exhaust flow as a solid body issuing from the ejector exit. For small angles of attack, only upper surface areas very near the leading edge showed significant differences when compared with cases without the exhaust simulated, and the inlet flow field was virtually unchanged. Therefore, an accurate simulation of the inlet flow field at small values of $\alpha$ was believed to be obtained without developing a suitable model for a jet in a cross flow which is beyond the current capabilities of VSAERO. Also note, all VSAERO results presented here are inviscid.

## Computational Fluid Dynamics Results

Because of height control problems, all the experimental data obtained for the cruise configuration are in ground effects, and therefore, comparisons of experimental with computational results are presented only for the ejector configuration out of ground effect. Figure 37 shows the upper surface pressure distribution predicted by VSAERO for $q_\infty = 0$ psf, $\alpha = 0°$, and NPR = 2.5, and figure 38 shows the predicted surface pressure at $q_\infty = 12$ psf. Notice the predicted free-stream influence on the inlet flow entrainment pattern which actually creates a stagnation region aft of the ejectors. As interpreted from the experimental data, the entrainment is greatly increased between the ejectors and leading edge with wind on.

Figures 39 through 41 show the inlet pressure data at BL = 6.0 in. and FS = 57.2 in. (the ejector's midspan and midlength) with $\alpha = 0°$, NPR = 2.5, and $q_\infty = 0, 3$, and 12 psf, respectively. At $q_\infty = 0$ psf (fig. 39), excellent correlation with the experimental results is obtained on the BL, but the correlation along the FS is not as good. This difference may be an indication that the paneling needs to be extended farther into the inlet because the shape of the sidewalls creates the nozzle contraction. With wind on (figs. 40 and 41), the correlation with experimental data along the BL is still good; however, the inlet leading-edge suction peak is underpredicted. Along the FS, the predicted pressure on the inboard inlet lip closely matches the experimental data with a slight deviation at the peak. Again, the behavior of the predicted pressure at the peak indicates that the inlet paneling should be extended to resolve the suction peaks. Results from VSAERO on the outboard lip severely underpredict the suction peak, and this discrepancy grows with increasing $q_\infty$. Overall, the predicted pressures are reasonably good, but VSAERO has problems accurately predicting the level of suction peaks resulting from large flow entrainment, especially if the peaks are caused by cross-flow entrainment as is true for the outboard inlet lip.

Figure 42 shows the computed inlet velocities and the experimental inlet velocities as measured by the laser velocimetry technique described previously. The data are presented for $q_\infty = 3$ psf, $\alpha = 0°$, HGT = 32 in., and NPR = 2.5 with the velocity

vectors scaled and color-shaded by their ratio to the free-stream velocity magnitude. Because the laser velocimetry data consist only of the horizontal and vertical velocity components, the computed data presented likewise contains only these two components. In general, the velocity flow field is very accurately predicted with the largest differences occurring near the inlet lips. This is also where the largest standard deviation occurs in the LV measurements.

## Conclusions

A wind-tunnel investigation of a 20-percent-scale unmanned aerial vehicle model with an ejector system for powered lift was conducted in the Langley 14- by 22-Foot Subsonic Tunnel to examine the performance of an integrated ejector system. The model was tested from hover through transition conditions in and out of ground effects. Force, moment, and pressure data were obtained. A laser velocimeter (LV) technique was demonstrated. In addition, these data were used for correlation with computational fluid dynamics (CFD) predictions from the panel method, VSAERO. Conclusions drawn from the results of the wind-tunnel test and the CFD correlation are as follows:

1. Skewing the diffuser 10° downstream and adding forward and aft endplates between the diffusers to create a centerline dam significantly increases augmentaion ratio in ground effects and reduces the drag coefficient when out of ground effects with power on.

2. Although most inlet door designs have a detrimental effect on ejector performance, an aerodynamically shaped centerbody door design can actually improve ejector performance in ground effects and maintain the performance of the no door configuration out of ground effects.

3. Installation of diffuser turning vanes significantly decreased ejector performance with wind off. Except for slightly increasing drag, turning vane installation has surprisingly little effect on the vehicle aerodynamics with wind on. Symmetrical deflection of turning vanes produces significant amounts of forward thrust or drag while producing little pitching-moment coefficient ($C_m$). Unsymmetrical vane deflections produce directional control that is essentially uncoupled from roll.

4. Nose-up pitching moments were reduced by plugging the two forward primary nozzles. Adding a splitter plate between the plugged nozzles and the flowing nozzles did not further reduce $C_m$. This may be a result of poor design of the splitter plate. In either case, some of the resulting lift loss can be recovered by increasing primary nozzle pressure ratio without adversely affecting $C_m$.

5. An LV technique which measures only horizontal and vertical velocity components can be used to investigate the inlet flow field.

6. With wind off, excellent correlation between experimental results and VSAERO results can be obtained. With wind on, correlation is still good; however, the inlet leading-edge suction peak is underpredicted.

NASA Langley Research Center
Hampton, VA 23681-0001
January 20, 1993

## References

1. Fulghum, David A.: Gulf War Successes Push UAVs Into Military Doctrine Forefront. *Aviation Week & Space Technol.,* vol. 135, no. 23, Dec. 9, 1991, pp. 38–39.

2. Riley, Donald R.; Shah, Gautam H.; and Kuhn, Richard E.: *Low-Speed Wind-Tunnel Results of a 15-Percent-Scale Model of an E-7A STOVL Fighter Configuration.* NASA TM-4107, 1989.

3. Barankiewicz, Wendy S.: *Static Performance Tests of a Flight-Type STOVL Ejector.* NASA TM-104437, 1991.

4. Garland, D. B.; and Gilbertson, F. L.: A Review of the Scale Effects on the Static Performance of Lift Ejectors. AIAA-90-1819, Feb. 1990.

5. Gentry, Garl L., Jr.; Quinto, P. Frank; Gatlin, Gregory M.; and Applin, Zachary T.: *The Langley 14- by 22-Foot Subsonic Tunnel: Description, Flow Characteristics, and Guide for Users.* NASA TP-3008, 1990.

6. Paulson, John W., Jr.; Quinto, P. Frank; and Banks, Daniel W.: *Investigation of Trailing-Edge-Flap Spanwise-Blowing Concepts on an Advanced Fighter Configuration.* NASA TP-2250, 1984.

7. Sellers, William L.; and Elliott, Joe E.: Applications of a Laser Velocimeter in the Langley 4- by 7-Meter Tunnel. *Flow Visualization and Laser Velocimetry for Wind Tunnels,* William W. Hunter, Jr., and Jerome T. Foughner, Jr., eds., NASA CP-2243, 1982, pp. 283–293.

8. Riley, Donald R.; Shah, Gautam H.; and Kuhn, Richard E.: *Some Power-Induced Effects for Transition Flight Measured on a 15-Percent-Scale E-7A STOVL Fighter Model.* NASA TM-4188, 1990.

9. Maskew, Brian: Prediction of Subsonic Aerodynamic Characteristics: A Case for Low-Order Panel Methods. *J. Aircr.,* vol. 19, no. 2, Feb. 1982, pp. 157–163.

10. Steinbrenner, John P.; Chawner, John R.; and Fouts, Chris L.: *The Gridgen 3D Multiple Block Grid Generation System, Volume 1.* WRDC TR-90-3022-VOL-1, U.S. Air Force, July 1990. (Available from DTIC as AD B148 627L.)

Table I. Basic Model Geometry

| | |
|---|---|
| Wing-body: | |
| Aspect ratio | 2.12 |
| $S$, in$^2$ | 2 427.10 |
| $b$, in. | 71.72 |
| $\overline{c}$, in. | 41. 92 |
| Leading-edge sweep, deg | 60.00 |
| Trailing-edge sweep at— | |
| Root, deg | −37.50 |
| First trailing-edge break (BL = 12.3 in.), deg | 60.00 |
| Second trailing-edge break (BL = 21.6 in.), deg | −37.50 |
| Chord length at— | |
| Root, in. | 66.40 |
| First break, in. | 35.66 |
| Second break, in. | 35.66 |
| Airfoil section | Bicon vex |
| Cross-sectional area distribution | Figure 2 |
| Ejector (each): | |
| Length, in. | 19.20 |
| Depth (measured from throat), in. | 8.86 |
| Primary nozzle exit area, in$^2$ | 0.096 |
| Throat exit area, in$^2$ | 84.48 |
| Diffuser exit area, in$^2$ | 144.08 |
| Diffuser exit WL, in. | 11.43 |

Figure 1. Three-view sketch of model and photograph of it installed in Langley 14- by 22-Foot Subsonic Tunnel.

L-93-05 Figure 2. Cross-sectional area distribution of 20-percent-scale model of UAV.

Figure 3. Cut-away view showing half of ejector system with balance in place.

(a) Baseline and skewed ejector configurations.

(b) Baseline ejector configuration with diffuser turning vanes installed.

Figure 4. Sketch of cross section cut through center of ejector (BL = 6.0 in.).

Figure 5. Sketch of flow field between two ejectors operating in ground effects.

(a) Outboard door design.

(b) Split inboard/outboard door design.

(c) Aerodynamically shaped centerbody door design.

Figure 6. Sketches of tested inlet door designs. Linear dimensions are in inches.

Figure 7. Baseline ejector performance. $q_\infty = 0$ psf; HGT = 32 in.

Figure 8. Ground effects on baseline ejector performance. $q_\infty = 0$ psf; NPR = 2.5.

Figure 9. Baseline ejector augmentation. $q_\infty = 0$ psf; NPR = 2.5.

Figure 10. Baseline longitudinal aerodynamics. HGT = 32 in.

(a) Longitudinal aerodynamic coefficients.

Figure 11. Variation of baseline aerodynamics with NPR and $q_\infty$. HGT = 32 in.

(b) Ejector-induced effects over test range of $V_e$. $\alpha = 0°$.

Figure 11. Concluded.

Figure 12. Ground effects on baseline longitudinal aerodynamics. NPR = 2.5.

Figure 13. Effect of sideslip on baseline longitudinal aerodynamics at $\alpha = 0°$. HGT = 32 in.

Figure 14. Effect of sideslip on baseline longitudinal aerodynamics at $\alpha = 10°$. HGT = 32 in.

Figure 15. Effect of sideslip on lateral-directional aerodynamics. $\alpha = 0°$; HGT = 32 in.

Figure 16. Effect of sideslip on lateral-directional aerodynamics at $\alpha = 10°$. HGT = 32 in.

Figure 17. Effect of forward endplates on ejector augmentation. $q_\infty = 0$ psf; $\alpha = 0°$; NPR = 2.5.

Figure 18. Effect of forward endplates on longitudinal aerodynamics. $q_\infty = 12$ psf; HGT = 32 in.

Figure 19. Effect of diffuser skew and centerline dam on ejector augmentation at $\alpha = 0°$. $q_\infty = 0$ psf; NPR = 2.5.

Figure 20. Effect of diffuser skew and centerline dam on ejector augmentation at $\alpha = 10°$. $q_\infty = 0$ psf; NPR = 2.5.

Figure 21. Effect of diffuser skew and centerline dam on longitudinal aerodynamics. $q_\infty = 12$ psf; HGT = 32 in.

Figure 22. Effect of inlet door design on ejector performance. $q_\infty = 0$; $\alpha = 0°$; HGT = 32 in.

Figure 23. Effect of inlet door design on ejector augmentation at $\alpha = 0°$. $q_\infty = 0$ psf; NPR = 2.5.

Figure 24. Effect of inlet door design on ejector augmentation at $\alpha = 10°$. $q_\infty = 0$ psf; NPR = 2.5.

Figure 25. Effect of inlet door design on longitudinal aerodynamics. $q_\infty = 12$ psf; HGT = 32 in.

Figure 26. Effect of ejector inlet door design on longitudinal aerodynamics with sideslip. $q_\infty = 12$ psf; $\alpha = 0°$; HGT = 32 in.; NPR = 2.5.

Figure 27. Effect of ejector inlet door design on lateral-directional aerodynamics with sideslip. $q_\infty = 12$ psf; $\alpha = 0°$; HGT = 32 in.; NPR = 2.5.

Figure 28. Effect of diffuser turning vane installation. $q_\infty = 0$ psf; $\alpha = 0°$; NPR = 2.5.

Figure 29. Effect of diffuser turning vane installation on longitudinal aerodynamics. $q_\infty = 12$ psf; HGT = 32 in.

Figure 30. Effect of diffuser turning vane deflection on longitudinal aerodynamics. $q_\infty = 12$ psf; HGT = 32 in.; NPR = 2.5; forward endplates removed.

Figure 31. Effect of unsymmetrical diffuser turning vane deflection on ejector performance. $q_\infty = 0$ psf; $\alpha = 0°$; NPR = 2.5; forward endplates removed.

Figure 32. Lateral-directional control using turning vanes. $q_\infty = 0$ psf; $\alpha = 0°$; NPR = 2.5; forward endplates removed.

Figure 33. Effect of unsymmetric diffuser turning vane deflection on longitudinal aerodynamics. $q_\infty = 12$ psf; HGT = 32 in.; NPR = 2.5; forward endplates removed.

Figure 34. Lateral-directional control using diffuser turning vanes. $q_\infty = 12$ psf; HGT = 32 in.; NPR = 2.5; forward endplates removed.

Figure 35. Effect of plugged nozzles and splitter plate on longitudinal aerodynamics. $q_\infty = 12$ psf; HGT = 32 in.; ejector skewed 10°.

Figure 36. Panel representation of UAV ejector configuration used in VSAERO analysis.

Figure 37. Surface $C_{p,e}$ distribution as predicted by VSAERO for $q_\infty = 0$ psf, $\alpha = 0°$, NPR = 2.5, and HGT = 32 in.

Figure 38. Surface $C_p$ distribution predicted by VSAERO for $q_\infty = 12$ psf, $\alpha = 0°$, NPR = 2.5, and HGT = 32 in.

Figure 39. Inlet pressure data for $q_\infty = 0$ psf, $\alpha = 0°$, NPR = 2.5, and HGT = 32 in.

Figure 40. Inlet pressure data for $q_\infty = 3$ psf, $\alpha = 0°$, NPR = 2.5, and HGT = 32 in.

Figure 41. Inlet pressure data for $q_\infty = 12$ psf, $\alpha = 0°$, NPR = 2.5, and HGT = 32 in.

(a) Velocity vectors predicted by VSAERO.

(b) Experimental velocity vectors measured by laser velocimetry.

Figure 42. Two-dimensional inlet velocity vectors on vertical plane located at BL = 6 in. $q_\infty = 3$ psf; $\alpha = 0°$; NPR = 2.5; HGT = 32 in.

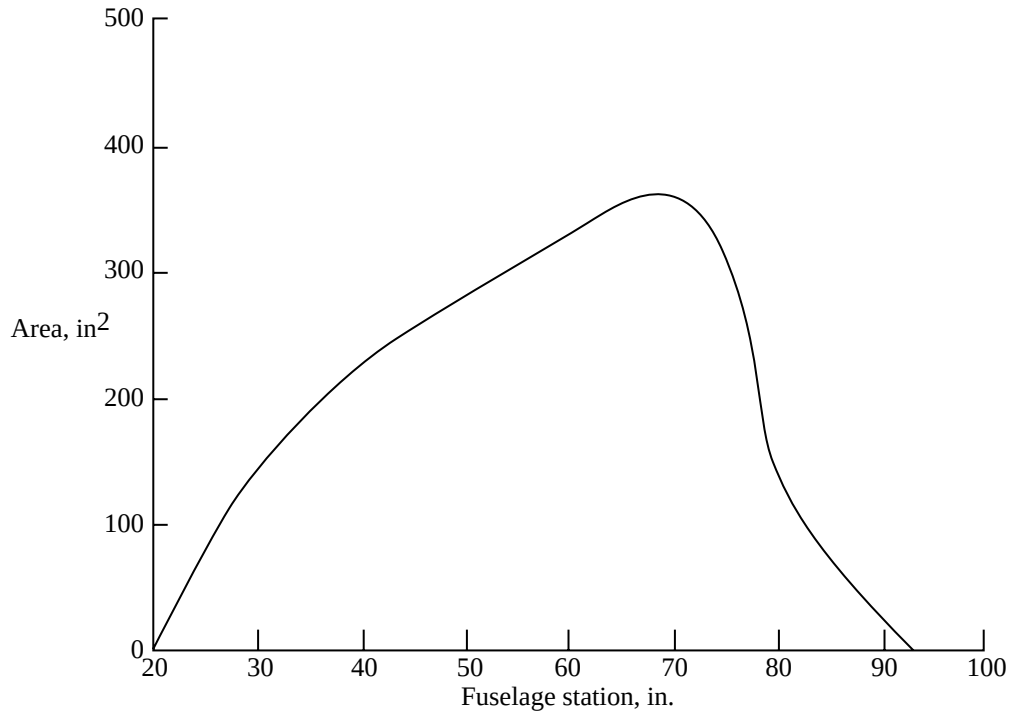


Figure 2. Cross-sectional area distribution of 20-percent-scale model of UAV.

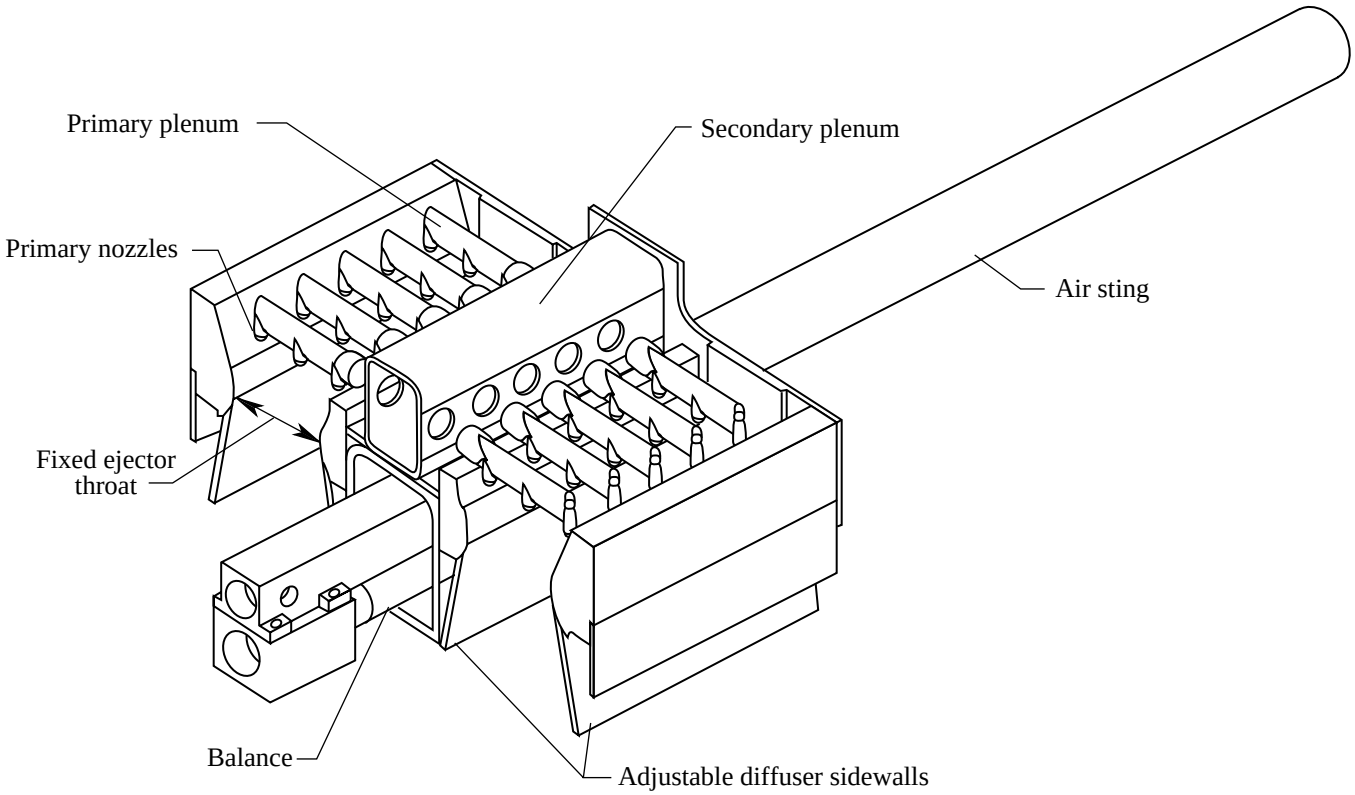


Figure 3. Cut-away view showing half of ejector system with balance in place.

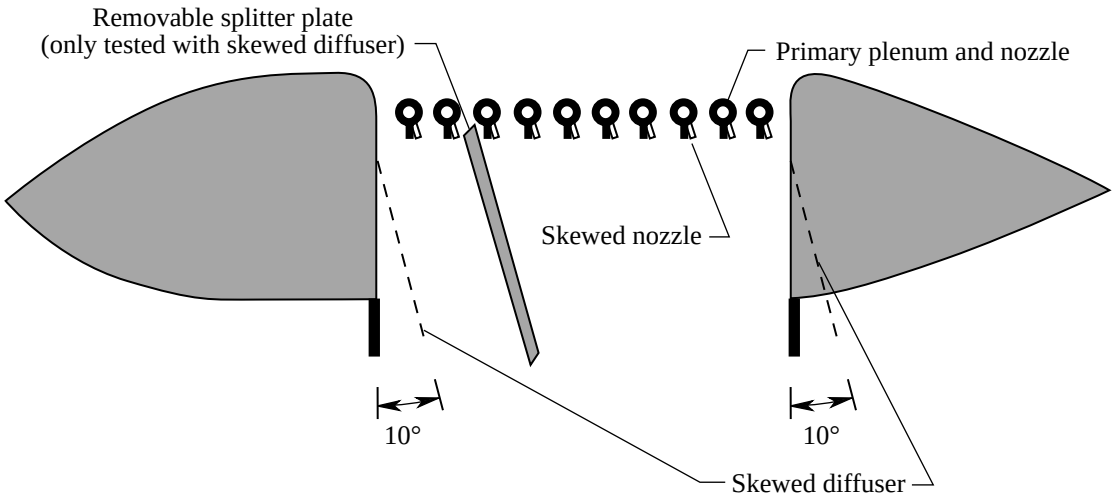


(a) Baseline and skewed ejector configurations.

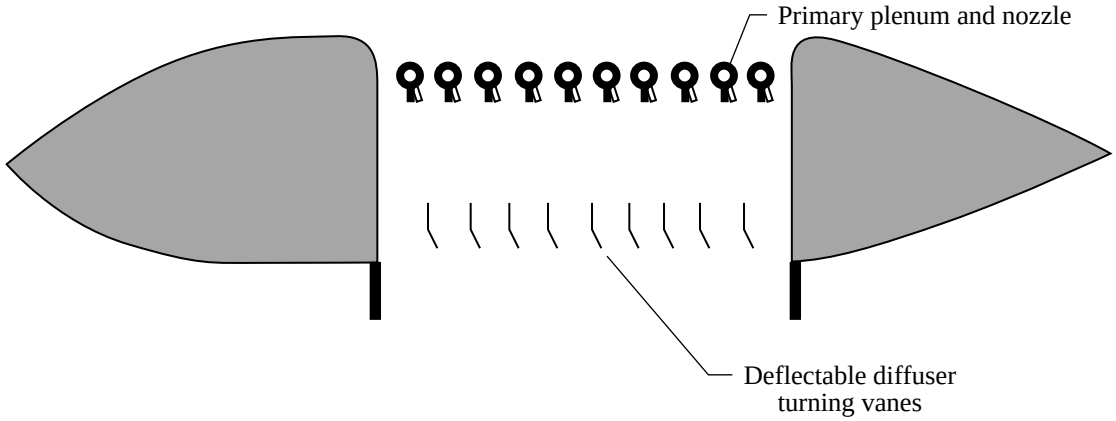


(b) Baseline ejector configuration with diffuser turning vanes installed.

Figure 4. Sketch of cross section cut through center of ejector (BL = 6.0 in.).

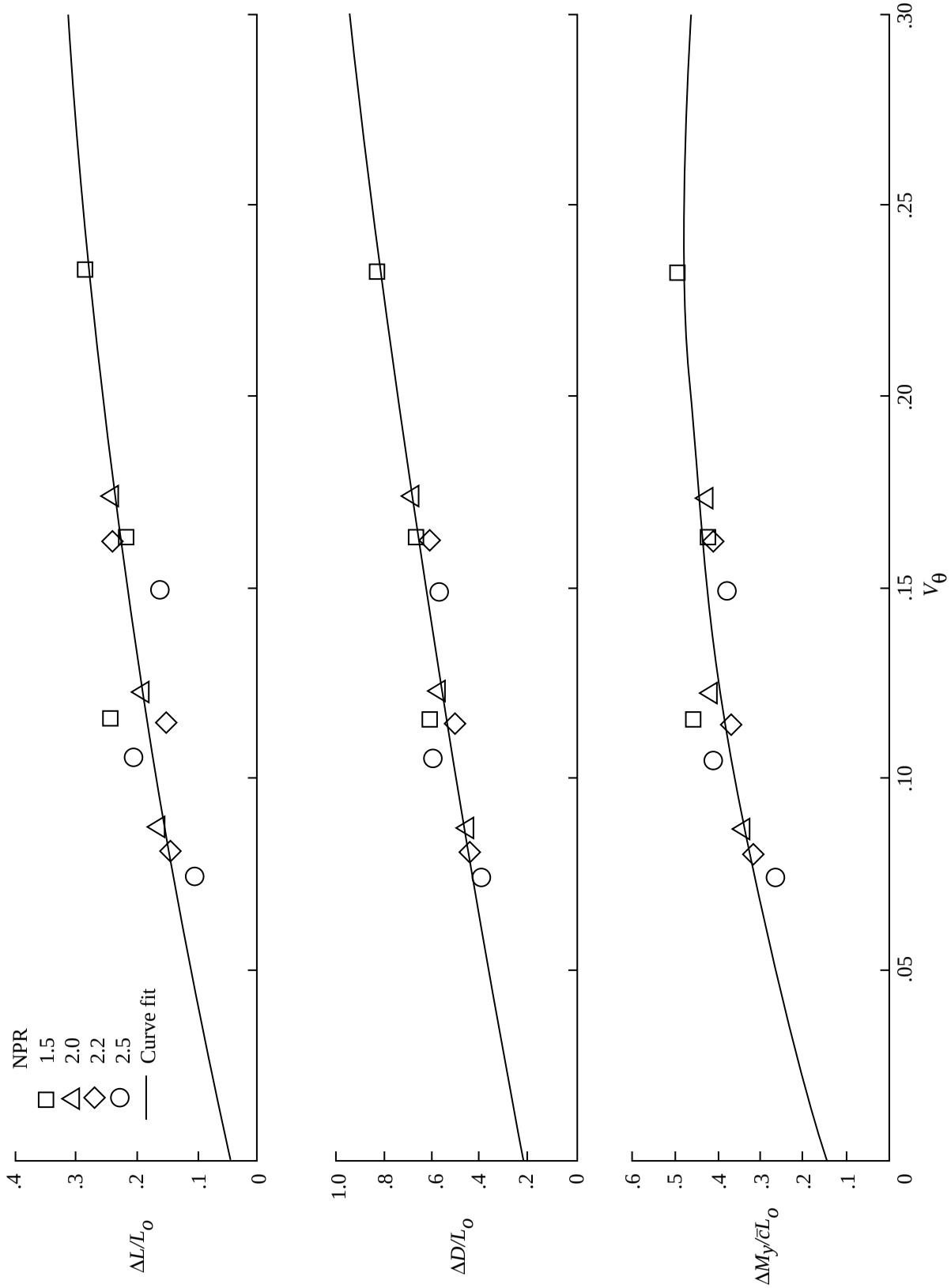


(b) Ejector induced effects over test range of $V_e$. $\alpha = 0°$

Figure 11. Concluded.

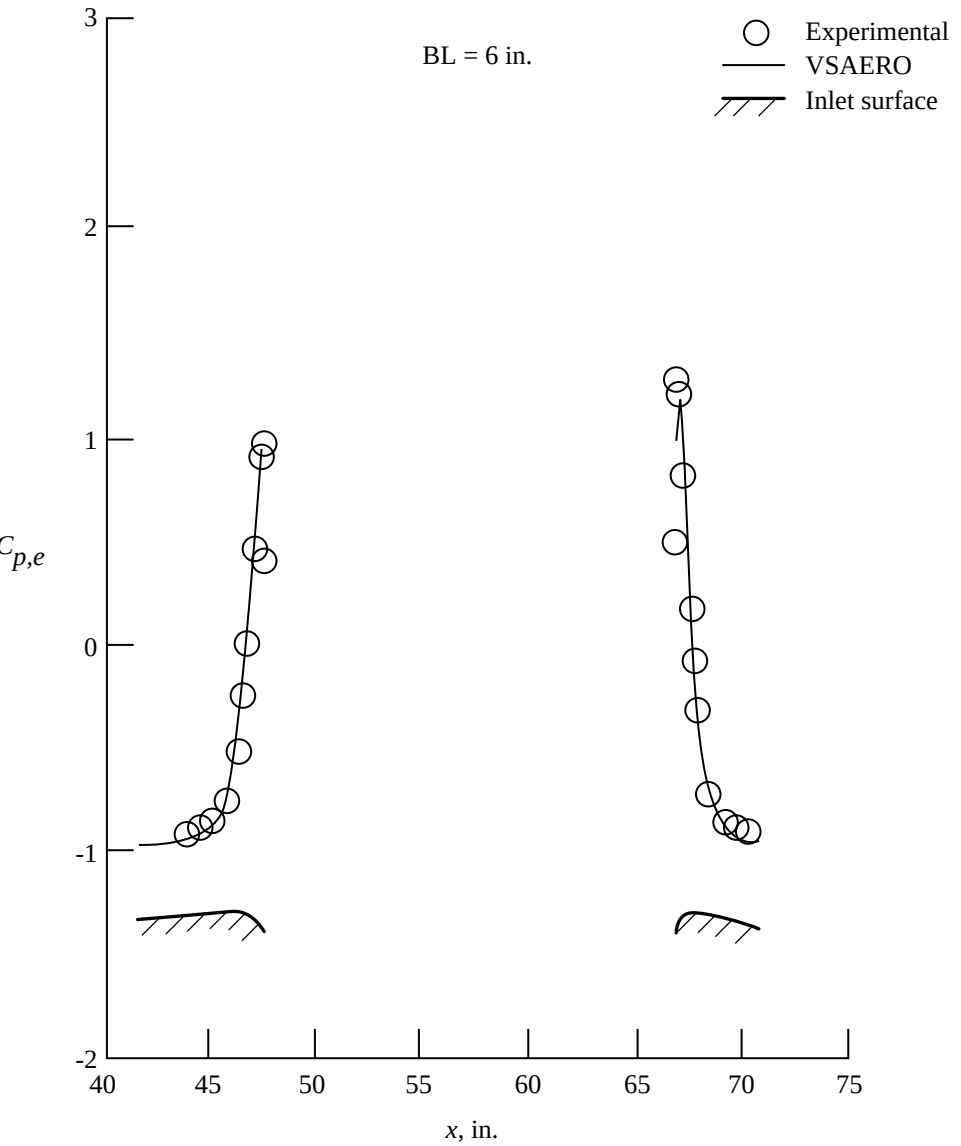
BL = 6 in.
Experimental
VSAERO
Inlet surface
3
2
1
0
-1
-2
$-C_{p,e}$
40
45
50
55
60
65
70
75
$x$, in.

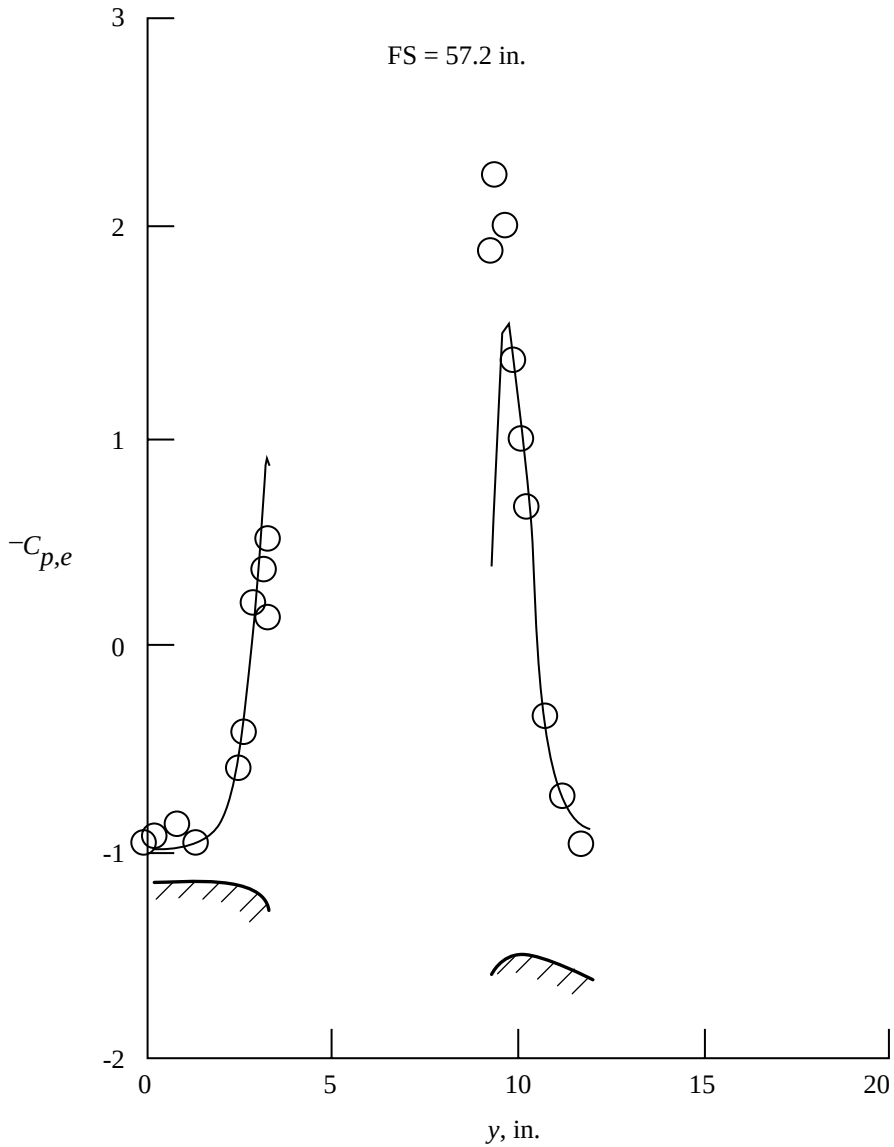
FS = 57.2 in.
3
2
1
0
-1
-2
$-C_{p,e}$
0
5
10
15
20
$y$, in.

Figure 39. Inlet pressure data for $q_\infty = 0$ psf, $\alpha = 0^o$, NPR = 2.5, and HGT = 32 in.

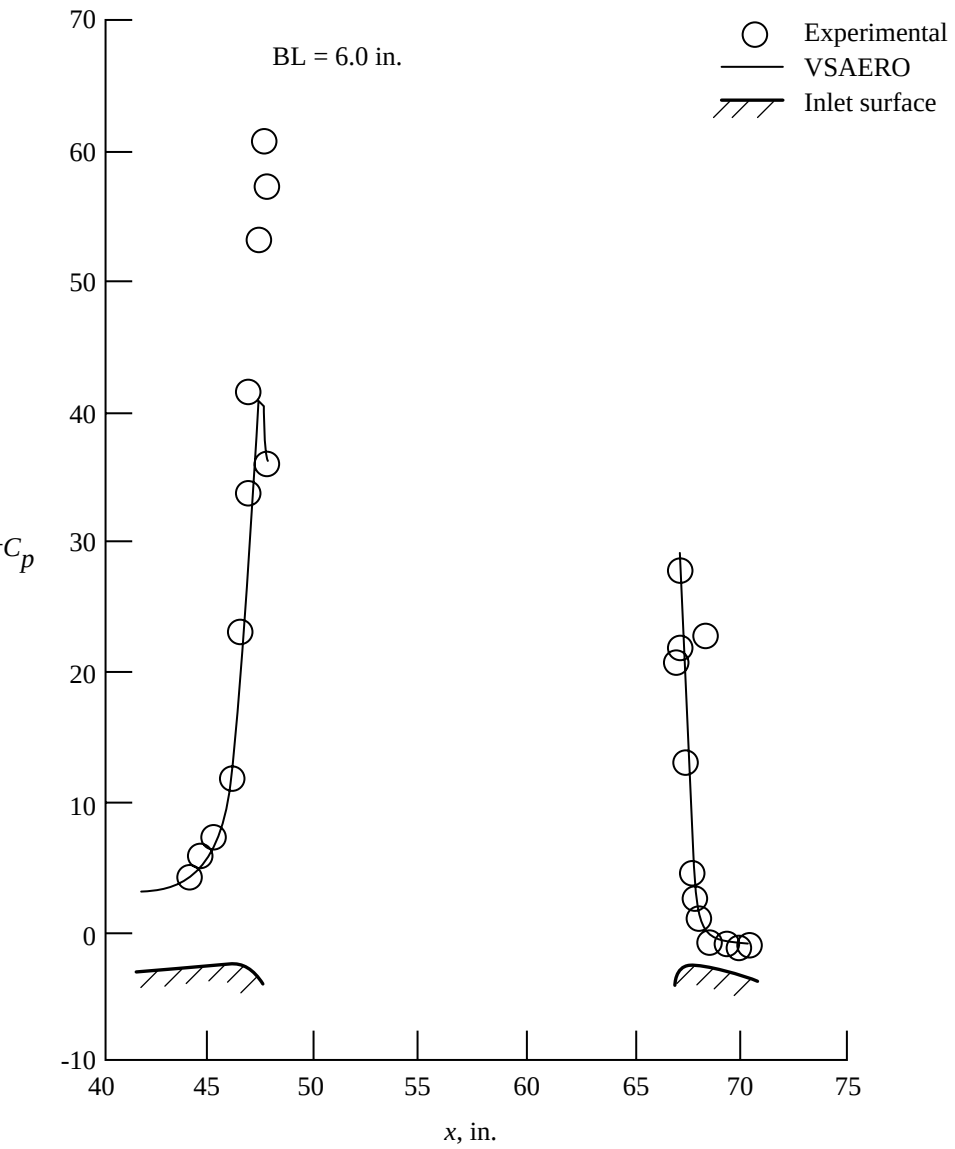
BL = 6.0 in.
Experimental
VSAERO
Inlet surface
70
60
50
40
30
20
10
0
-10
$-C_p$
40
45
50
55
60
65
70
75
$x$, in.

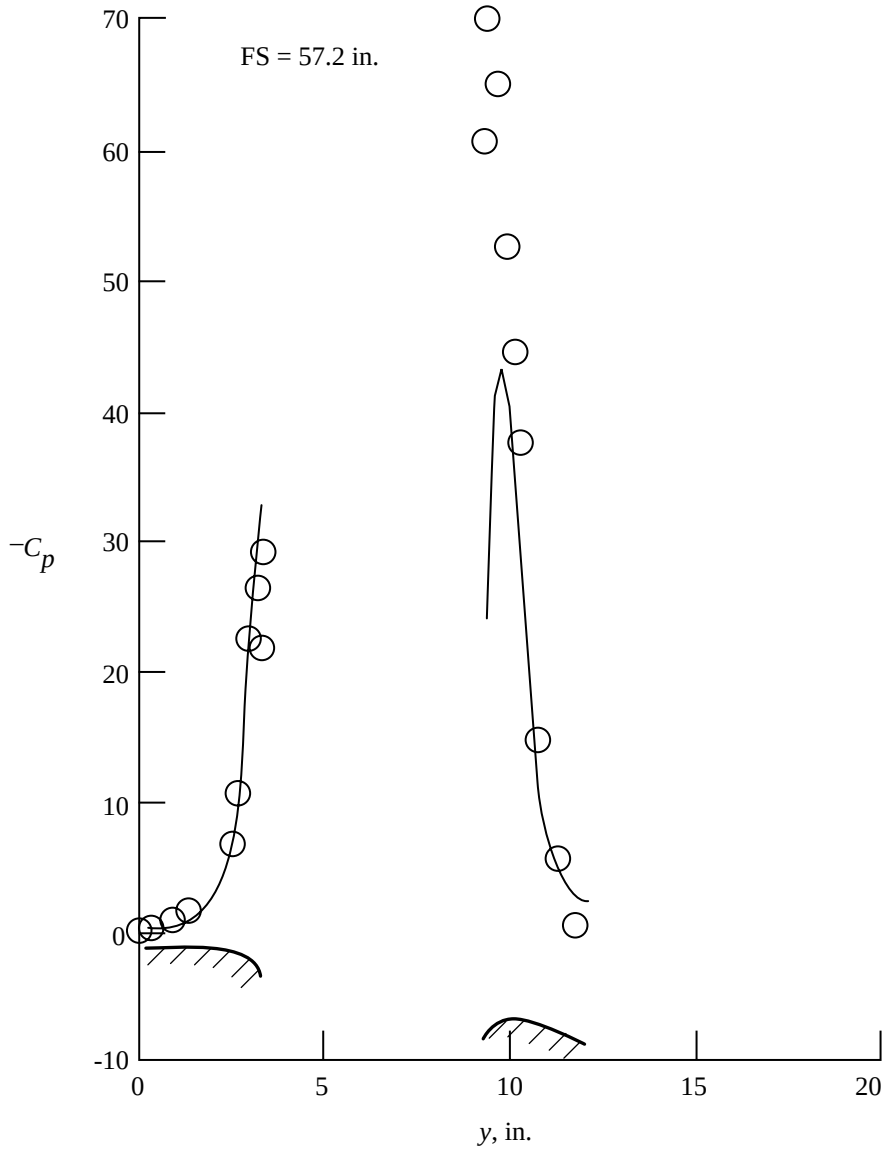
FS = 57.2 in.
70
60
50
40
30
20
10
0
-10
$-C_p$
0
5
10
15
20
$y$, in.

Figure 40. Inlet pressure data for $q_\infty = 3$ psf, $\alpha = 0^\circ$, NPR = 2.5, and HGT = 32 in.

BL = 6 in.
Experimental
VSAERO
Inlet surface
$-C_p$
30
25
20
15
10
5
0
-5
-10
40
45
50
55
60
65
70
75
$x$, in.


FS = 57.2 in.
$-C_p$
30
25
20
15
10
5
0
-5
-10
0
5
10
15
20
$y$, in.

Figure 41. Inlet pressure data for $q_\infty = 12$ psf, $\alpha = 0^\circ$, NPR = 2.5, and HGT = 32 in.

# REPORT DOCUMENTATION PAGE

*Form Approved*
*OMB No. 0704-0188*

Public reporting burden for this collection of information is estimated to average 1 hour per response, including the time for reviewing instructions, searching existing data sources, gathering and maintaining the data needed, and completing and reviewing the collection of information. Send comments regarding this burden estimate or any other aspect of this collection of information, including suggestions for reducing this burden, to Washington Headquarters Services, Directorate for Information Operations and Reports, 1215 Jefferson Davis Highway, Suite 1204, Arlington, VA 22202-4302, and to the Office of Management and Budget, Paperwork Reduction Project (0704-0188), Washington, DC 20503.

| 1. AGENCY USE ONLY *(Leave blank)* | 2. REPORT DATE | 3. REPORT TYPE AND DATES COVERED |
|---|---|---|
| | April 1993 | Technical Memorandum |

**4. TITLE AND SUBTITLE**
Transition Aerodynamics for 20-Percent-Scale VTOL Unmanned Aerial Vehicle

**5. FUNDING NUMBERS**
WU 505-59-30-02

**6. AUTHOR(S)**
Kevin J. Kjerstad and John W. Paulson, Jr.

**7. PERFORMING ORGANIZATION NAME(S) AND ADDRESS(ES)**
NASA Langley Research Center
Hampton, VA 23681-0001

**8. PERFORMING ORGANIZATION REPORT NUMBER**
L-17112

**9. SPONSORING/MONITORING AGENCY NAME(S) AND ADDRESS(ES)**
National Aeronautics and Space Administration
Washington, DC 20546-0001

**10. SPONSORING/MONITORING AGENCY REPORT NUMBER**
NASA TM-4419

**11. SUPPLEMENTARY NOTES**

**12a. DISTRIBUTION/AVAILABILITY STATEMENT**
Unclassified–Unlimited

Subject Category 02

**12b. DISTRIBUTION CODE**

**13. ABSTRACT** *(Maximum 200 words)*

An investigation was conducted in the Langley 14- by 22-Foot Subsonic Tunnel to establish a transition data base for an unmanned aerial vehicle utilizing a powered-lift ejector system and to evaluate alterations to the ejector system for improved vehicle performance. The model used in this investigation was a 20-percent-scale, blended-body, arrow-wing configuration with integrated twin rectangular ejectors. The test was conducted from hover through transition conditions with variations in angle of attack, angle of sideslip, free-stream dynamic pressure, nozzle pressure ratio, and model ground height. Force and moment data along with extensive surface pressure data were obtained. A laser velocimeter technique for measuring inlet flow velocities was demonstrated at a single flow condition, and also a low order panel method was successfully used to numerically simulate the ejector inlet flow.

| 14. SUBJECT TERMS | 15. NUMBER OF PAGES |
|---|---|
| Powered lift; Ejectors; VTOL; Unmanned; Ground effects; CFD; Laser velocimetry (LV) | 49 |
| | **16. PRICE CODE** A03 |

| 17. SECURITY CLASSIFICATION OF REPORT | 18. SECURITY CLASSIFICATION OF THIS PAGE | 19. SECURITY CLASSIFICATION OF ABSTRACT | 20. LIMITATION OF ABSTRACT |
|---|---|---|---|
| Unclassified | Unclassified | | |

NSN 7540-01-280-5500

**Standard Form 298(Rev. 2-89)**
Prescribed by ANSI Std. Z39-18
298-102

NASA-Langley, 1993